

Third-order intermodulation distortion in graphene resonant channel transistors

Michael Lekas, Sunwoo Lee, Wujoon Cha, James Hone, and Kenneth Shepard

Citation: [Applied Physics Letters](#) **106**, 073504 (2015); doi: 10.1063/1.4913462

View online: <http://dx.doi.org/10.1063/1.4913462>

View Table of Contents: <http://scitation.aip.org/content/aip/journal/apl/106/7?ver=pdfcov>

Published by the [AIP Publishing](#)

Articles you may be interested in

[Enhanced force sensitivity and noise squeezing in an electromechanical resonator coupled to a nanotransistor](#)
Appl. Phys. Lett. **97**, 253105 (2010); 10.1063/1.3528454

[Synchronous measurement of even and odd order intermodulation distortion at the resonant frequency of a superconducting resonator](#)

Rev. Sci. Instrum. **81**, 024701 (2010); 10.1063/1.3301425

[Monte Carlo based analysis of intermodulation distortion behavior in GaN-Al x Ga 1-x N high electron mobility transistors for microwave applications](#)


J. Appl. Phys. **90**, 3030 (2001); 10.1063/1.1390495





[Origin of nonlinear surface impedance and intermodulation distortion in YBa 2 Cu 3 O 7-x microstrip resonator](#)

J. Appl. Phys. **86**, 5788 (1999); 10.1063/1.371594

[Critical-state model for intermodulation distortion in a superconducting microwave resonator](#)

J. Appl. Phys. **83**, 5307 (1998); 10.1063/1.367356


Instruments for Advanced Science

<p>Contact Hiden Analytical for further details: www.HidenAnalytical.com info@hiden.co.uk</p> <p>CLICK TO VIEW our product catalogue</p>	 <p>Gas Analysis</p> <ul style="list-style-type: none"> › dynamic measurement of reaction gas streams › catalysis and thermal analysis › molecular beam studies › dissolved species probes › fermentation, environmental and ecological studies 	 <p>Surface Science</p> <ul style="list-style-type: none"> › UHV TPD › SIMS › end point detection in ion beam etch › elemental imaging - surface mapping 	 <p>Plasma Diagnostics</p> <ul style="list-style-type: none"> › plasma source characterization › etch and deposition process reaction › kinetic studies › analysis of neutral and radical species 	 <p>Vacuum Analysis</p> <ul style="list-style-type: none"> › partial pressure measurement and control of process gases › reactive sputter process control › vacuum diagnostics › vacuum coating process monitoring
--	--	--	--	--

Third-order intermodulation distortion in graphene resonant channel transistors

Michael Lekas,¹ Sunwoo Lee,¹ Wujoon Cha,² James Hone,² and Kenneth Shepard^{1,a)}

¹Department of Electrical Engineering, Columbia University, New York, New York 10027, USA

²Department of Mechanical Engineering, Columbia University, New York, New York 10027, USA

(Received 26 December 2014; accepted 9 February 2015; published online 20 February 2015)

Third-order intermodulation distortion (IM3) is an important metric for electromechanical resonators used in radio frequency signal processing applications since it characterizes the nonlinearity of the device, and the amount of in-band interference it generates when subject to unwanted, out-of-band signals. In this letter, we measure and model IM3 in a strain-engineered graphene mechanical resonator operated as a graphene resonant channel transistor (G-RCT). The device analyzed in this work has a voltage third-order intercept point (V_{IIP3}) of 69.5 dBm V at a gate-to-source DC bias (V_{gs}) of 2.5 V, which drops to 52.1 dBm V at $V_{gs} = 4.5$ V when driven with two out-of-band input tones spaced 5 and 10 MHz from the resonant frequency. The decrease in the V_{IIP3} with V_{gs} coincides with an increase in the transmission response (S_{21}) of the device, illustrating a trade-off between transduction efficiency and linearity. In addition, we find that conventional micro-electro-mechanical systems theory for IM3 calculation does not accurately describe our measurement data. To resolve this discrepancy, we develop a model for IM3 in G-RCTs that takes into account all of the output current terms present in the embedded transistor structure, as well as an effective Duffing parameter (α_{eff}). © 2015 AIP Publishing LLC.

[<http://dx.doi.org/10.1063/1.4913462>]

Recently, nano-electro-mechanical system (NEMS) resonators made from graphene have generated a great deal of interest owing to graphene's unique electrical and mechanical properties, with application to sensing and radio-frequency (RF) circuits. The high breaking strength of graphene (34 N/m)¹ has made it possible to engineer large strains into suspended membranes, simultaneously boosting their resonant frequencies (f_0) and quality factors (Q) above 200 MHz and 200, respectively.^{2–4} Furthermore, the high room temperature carrier mobility of graphene (intrinsic $\mu > 10\,000\text{ cm}^2/\text{V}\cdot\text{s}$)⁵ allows resonators to be operated as three-terminal graphene resonant channel transistors (G-RCTs),⁶ which greatly amplifies the mechanical resonance signal of the device. This use of active sensing also obviates additional capacitive parasitics that degrade the rejection of off-resonance signals that plagues passive devices such as silicon micro-electro-mechanical systems resonators (Si-MEMS).⁷

Previous work on graphene resonators has focused on their behavior when actuated by a driving force at a single frequency. This includes studies on the relationship between the resonator size and its Q under linear operating conditions,^{8–10} as well as several other studies on higher-order mechanical nonlinearity.^{11–13} These latter studies concentrated on third-order nonlinearities, which are a function of the cubic, or Duffing, elastic constant (α_{eff}). Accurately predicting the value of α_{eff} under different operating conditions is critical for signal processing applications using graphene resonators because it dictates the onset of resonance bistability and sets the upper limit on the dynamic range of the device.

Although studies with single-frequency stimulus are essential for understanding the physical behavior of a resonator in applications like oscillator circuits¹⁴ and mass sensing,¹⁰ there are also many instances where the nonlinear behavior of the device in the presence of two or more input forces at different frequencies is of equal importance. An example of this is when a resonator is operated as a filtering element in an electronic system, passing signals near f_0 (its passband) and blocking signals away from f_0 . In this application, a resonator is subject to many different frequencies simultaneously, such that any nonlinearity in the device will create mixing products of the input tones that will appear at its output in addition to its linear response. This is problematic when two closely spaced tones located at f_1 and f_2 create third-order mixing products, known as third-order intermodulation distortion (IM3), that are located at $(2f_1 - f_2)$ and $(2f_2 - f_1)$. IM3 may be extremely detrimental in an RF filter because these product frequencies may fall at f_0 and overwhelm the desired passband signal.

Thin-film bulk acoustic resonators (FBARs) are currently the technology of choice for RF filter design due to their high Q s, multi-GHz f_0 ,¹⁵ and low IM3. Nonetheless, modern wireless applications generally require filter technologies to cover many different frequencies while consuming minimal die area, and FBARs are extremely limited in this regard since they are relatively large structures (100s of μm^2). Moreover, because f_0 is defined by film thickness, scaling FBARs for multi-frequency operation is challenging since a new deposition step must be added to the fabrication process for every additional frequency a chip must cover. While G-RCTs have demonstrated lower Q s than FBARs, they are an order of magnitude or more smaller, have much higher tunability, and their f_0 is a function of lateral

^{a)}Electronic mail: shepard@ee.columbia.edu

dimensions that are lithographically defined, allowing multi-frequency arrays of devices to be fabricated with a single deposition step. Still, IM3 is a concern for G-RCTs.

Despite its practical importance, there has been no study characterizing IM3 in resonators based on 2D materials. To address this, this letter presents measurements and theoretical analysis of IM3 in G-RCTs. Fig. 1(a) shows a scanning electron microscope (SEM) image and Fig. 1(b) shows a cross-sectional diagram of the strain-engineered G-RCT structure² analyzed in this paper. Briefly, the device consists of a graphene sheet suspended above a metal gate by source and drain electrodes made from e-beam deposited palladium, capped by gold. An SU-8 polymer clamp is lithographically patterned on top of the suspended graphene channel in a circular drum configuration. After SU-8 patterning, the devices are hard-baked at 250 °C to crosslink the polymer, causing it to shrink and apply additional strain to the suspended membrane. A more detailed description of the device fabrication and operating principle has been described elsewhere.²

All experiments were conducted in a Desert Cryogenics TTP4 vacuum probe station at $P_0 < 10^{-6}$ Torr, using GGB Industries GSG RF probes. Fig. 1(c) shows our measurement setup, which consists of two Agilent E8257C PSG Analog Signal Generators (SGs) that apply two input signals at $f_1 = f_0 - 2\Delta f$ and $f_2 = f_0 - \Delta f$, such that the nonlinearity in the G-RCT generates an IM3 tone at f_0 . The input signals are combined by a Mini-Circuits power combiner and fed into the gate of the G-RCT through the RF port of a bias-T. V_{gs} is applied through the DC port. The inputs to the combiner are preceded by 20-dB attenuators to isolate the SGs from one another to prevent IM3 from occurring in the sources themselves. A DC drain-to-source bias (V_{ds}) of 200 mV is applied on the DC port of a second bias-T to enable active sensing of

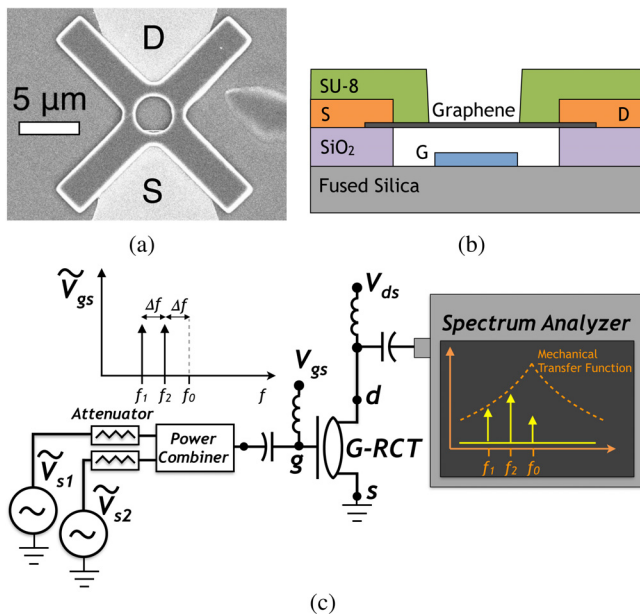


FIG. 1. (a) A SEM image of a G-RCT. The gate is not visible due to charging of the insulating substrate. (b) Cross sectional diagram of the device. The drain (D) and source (S) contacts are made from a stack of Ti/Pd/Au with thicknesses of 1/15/50 nm, respectively. The gate (G) is 50 nm of Pt. (c) IM3 measurement setup consisting of two RF sources feeding tones into the gate at $f_2 = f_0 - \Delta f$ and $f_1 = f_0 - 2\Delta f$, using a power combiner. The output power is measured at each frequency with a spectrum analyzer.

the resonance, while the output signal at the drain is fed from the RF port of the bias-T to the input of an Agilent E4440 spectrum analyzer. S-parameter (SP) measurements were also conducted on the device using an Agilent N5230A network analyzer in a standard two-port configuration.

Table I shows the dimensions and extracted parameters of the device analyzed in this work. Fig. 2(a) shows the measured magnitude of S_{21} as a function of the frequency and V_{gs} . The dashed line is a fit of the electrostatic frequency tuning characteristic using the continuum mechanics model for a 2D circular membrane,^{16–18} from which the effective mass (m_{eff}), the built-in strain due to the SU-8 clamp (σ), and the equilibrium deflection of the membrane (z_e) at each V_{gs} point are extracted. The value of m_{eff} is several times the intrinsic mass of the graphene membrane (m_0) due to residue from fabrication. Fig. 2(b) shows z_e as a function of V_{gs} demonstrating that the maximum z_e (~ 6 nm) is a small fraction of the overall gate-to-channel spacing at $V_{gs} = 0$ V ($z_0 = 115$ nm). The field-effect mobility μ_{FE} is extracted from low-field current-voltage measurements, where V_{ds} is set to 10 mV and V_{gs} is swept. Both μ_{FE} and Q were measured with $V_{gs} = 4.5$ V. We note that $Q \sim 120$ is relatively low compared to the large values observed at cryogenic temperatures in other work.¹² This study targets applications in consumer electronics, and therefore our experiments were conducted at room temperature where more sources of dissipation are present.

We measure the IM3 produced by the G-RCT by sweeping the voltage amplitude of the input tones (\tilde{V}_{gs}), and measuring the output signal at f_2 due to the linear response (\tilde{V}_{ds,f_2}), and at f_0 due to the IM3 product (\tilde{V}_{ds,f_0}). This measurement was repeated for a range of V_{gs} values. In order to avoid any unwanted effects due to possible drift of f_0 between IM3 measurements at each V_{gs} point, prior to each IM3 measurement a single tone was swept through the resonance and the response was measured with the spectrum analyzer to verify the location of f_0 . f_1 and f_2 were then set in reference to this value of f_0 so they could properly create an IM3 product at f_0 .

Figs. 3(a) and 3(b) show example IM3 measurements at two V_{gs} points. All of the output voltage amplitudes are referenced to 50 Ω , and all of the units are in dBm V for easier comparison with other high-impedance devices in the literature.^{19,20} In addition, the spacing of the input tones (Δf) for this measurement was set to 5 MHz—far enough from f_0 to avoid driving the device into bistability at higher \tilde{V}_{gs} , while close enough to f_0 to generate an IM3 tone that was above

TABLE I. Device parameters.

Parameter	Value
Channel length (L)	4 μm
Channel width (W)	6 μm
Diameter (D)	4 μm
Gate-to-channel spacing (z_0)	115 nm
Quality factor (Q)	120
Effective mass (m_{eff})	5.8 m_0
Strain (σ)	0.006
Mobility (μ_{FE})	885 $\text{cm}^2/\text{V}\cdot\text{s}$

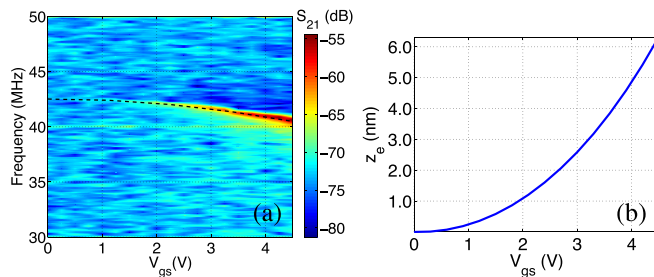


FIG. 2. (a) S_{21} as a function of frequency and V_{gs} . The dashed line represents a fit of the frequency tuning from the continuum mechanics model, which is used to extract m_{eff} , σ , and z_e . (b) Extracted z_e from the tuning fit.

the noise floor of our measurement system. The fit lines show that \tilde{V}_{dsf_0} and \tilde{V}_{dsf_2} have slopes of three and one, respectively, as predicted by theory. The value of \tilde{V}_{gs} at the intersection point of these lines is the input third-order intercept point (V_{IIP3}), a common metric for two-tone third-order nonlinearity.

Fig. 3(c) shows V_{IIP3} measurements at several V_{gs} bias points (red circles) in addition to those shown in Figs. 3(a) and 3(b). The data indicate that linearity in the G-RCT deteriorates as V_{gs} increases. Fig. 3(d) shows the measured magnitude of S_{21} as a function of frequency for several values of V_{gs} . This data demonstrate that the peak value of S_{21} increases approximately 40 dB per decade of increase in V_{gs} . The primary observation to be made from Figs. 3(c) and 3(d) is that there is a fundamental tradeoff between linearity and transduction in these devices, similar to that observed in other MEMS resonators.^{19,20} The electrostatic force on the

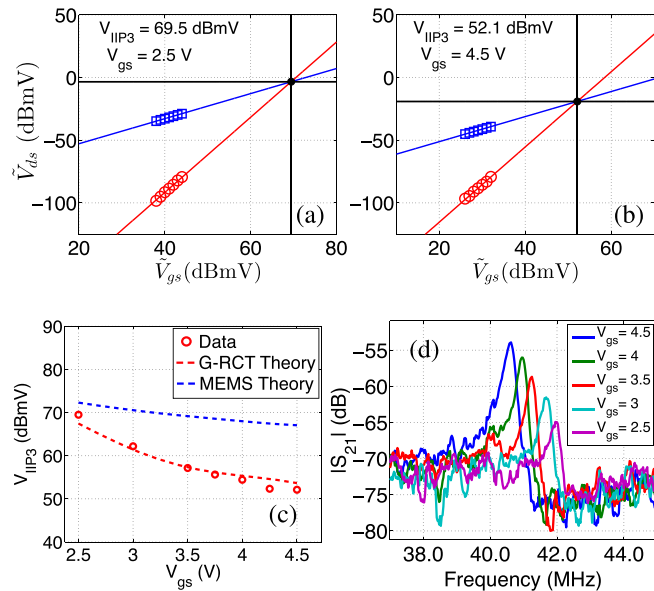


FIG. 3. (a) IM3 measurements taken at $V_{gs} = 2.5$ V and (b) $V_{gs} = 4.5$ V, with $\Delta f = 5$ MHz. \tilde{V}_{gs} is swept and the V_{IIP3} is measured as the value of \tilde{V}_{gs} at which the extrapolated first order (blue line) and third order (red line) output amplitudes intersect. Units are in voltage (dBm V) rather than power since the G-RCT has a high input impedance. (c) Measurements of V_{IIP3} as a function of V_{gs} (red circles), including two fits: one using previous MEMS theory and assuming nonlinearity only in the capacitive force (dashed blue line), and the other using the new G-RCT theory with extracted values of α_{eff} (red dashed line). (d) S_{21} as a function of frequency for different values of V_{gs} . The peak value of S_{21} increases approximately 40 dB per decade of increase in V_{gs} , due to the fact that $S_{21} \propto V_{gs}^2$.

graphene is independent of the position of the Dirac point so the gate-bias may always be set to maximize the transconductance in order to improve transduction. However, although increasing V_{gs} improves transduction, it also increases nonlinear forces as the membrane deflects further and degrades V_{IIP3} .

Previous theoretical analyses of IM3 in electromechanical resonators only account for nonlinearity in the capacitive force and ignore the effects of static displacement.^{19,20} The blue dashed line in Fig. 3(c) is a fit of V_{IIP3} using this formulation, which does not accurately model V_{IIP3} for a G-RCT. We improve this fit by developing a model for V_{IIP3} based on values of α_{eff} extracted from measurement. Figs. 4(a) and 4(b) show measurements of the G-RCT output current (i_o) as a function of frequency with \tilde{V}_{gs} swept, for two different values of V_{gs} . The value of \tilde{V}_{gs} at the onset of bistability ($\tilde{V}_{gs,crit}$) observed in this measurement can be used to calculate the motional amplitude at the onset (z_{crit}) using the transfer function given by Xu *et al.*²¹ The resulting values of z_{crit} as a function of V_{gs} are shown in Fig. 4(c). In the limit of weak nonlinearity²²

$$\alpha_{eff} = 1.54 \frac{m_{eff} \omega_0^2}{Q z_{crit}}, \quad (1)$$

where $\omega_0 = 2\pi f_0$. The values of α_{eff} calculated with this expression are also shown in Fig. 4(c).

V_{IIP3} can then be calculated by equating the output current terms at f_2 with the motional IM3 output current at f_0 , and solving for \tilde{V}_{gs} ²¹

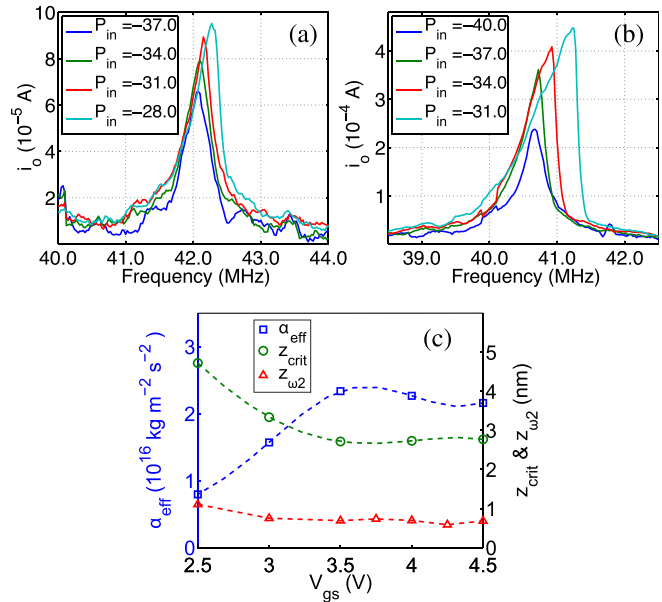


FIG. 4. Output current (i_o) as a function of frequency with varying input drive for (a) $V_{gs} = 2.5$ V and (b) $V_{gs} = 4.5$ V. i_o is calculated from S-parameter measurements, and the value of \tilde{V}_{gs} at the onset of bistability (calculated from the network analyzer drive power) is used to extract z_{crit} and α_{eff} . The units for drive power are dBm. (c) α_{eff} , $\tilde{z}_{\omega 2}$, and z_{crit} as a function of V_{gs} . The symbols on the α_{eff} and z_{crit} traces indicate points where $\tilde{V}_{gs,crit}$ was measured, and the line is a third order polynomial fit that was used for interpolation when calculating α_{eff} at some V_{gs} points. $\tilde{z}_{\omega 2}$ was lower than z_{crit} at all bias points.

$$\begin{aligned}
& -j\omega_0 \frac{\tilde{z}_{\omega 0}}{z_{0,e}} C_g V_{gs} + g_m \frac{\tilde{z}_{\omega 0}}{z_{0,e}} V_{gs} \\
& = -j\omega_2 C_{FT} \tilde{V}_{gs} - j\omega_2 \frac{\tilde{z}_{\omega 2}}{z_{0,e}} C_g V_{gs} + g_m \tilde{V}_{gs} + g_m \frac{\tilde{z}_{\omega 2}}{z_{0,e}} V_{gs}, \quad (2)
\end{aligned}$$

where g_m is the transconductance calculated from the μ_{FE} extracted from low-field current-voltage measurements, $z_{0,e} = z_0 - z_e$, C_g is the gate-to-channel capacitance of the suspended area of the graphene, $\omega_2 = 2\pi f_2$, and C_{FT} is the total gate-to-drain feedthrough capacitance which we approximate as being equal to the total gate-to-channel capacitance of the graphene ($C_{g,tot} = \epsilon_0 WL/z_0$) since our device has an RF layout with low parasitic capacitance. The first term on the left hand side of Eq. (2) is the passive displacement current observed in all vibrating MEMS devices, and the second term is the actively transduced mechanical signal. Electrical feedthrough currents, represented by the first and third terms on the right hand side of Eq. (2), are not present on the left hand side since the IM3 current is entirely due to the nonlinear actuating force. If the G-RCT is operated as either a p-channel device with negative V_{ds} or as a n-channel device with positive V_{ds} , the sign of g_m is positive.²¹ In addition, we use the sign convention that positive small signal current is flowing into the drain of the device.

$\tilde{z}_{\omega 0}$ is the motional amplitude at the IM3 frequency, which can be calculated with the following expressions:²³

$$\tilde{z}_{\omega 0} = -j \frac{F_{\omega 0,IM3} Q}{k_{eff}}, \quad (3)$$

$$F_{\omega 0,IM3} = \alpha_{eff} \frac{3}{4} \tilde{z}_{\omega 1} \tilde{z}_{\omega 2}^2, \quad (4)$$

where $F_{\omega 0,IM3}$ is the nonlinear IM3 force at f_0 , $\tilde{z}_{\omega 1}$ and $\tilde{z}_{\omega 2}$ are the motional amplitudes at f_1 and f_2 calculated with the same transfer function from Ref. 21, and k_{eff} is the spring constant of the system calculated from the continuum mechanics model. The solution of (2) yields the improved fit shown in Fig. 3(c) (red dashed line). To ensure the validity of our analysis, we also calculate $\tilde{z}_{\omega 2}$ at each V_{gs} point for the highest value of \tilde{V}_{gs} used during the IM3 measurements to confirm that the input tones were not driving the resonator beyond z_{crit} . As anticipated, Fig. 4(c) shows that $\tilde{z}_{\omega 2}$ is less than z_{crit} for all V_{gs} bias points.

The values of V_{IIP3} measured for this G-RCT are similar to those measured for contour-mode Si-MEMS devices, which offer analogous opportunities for integrating large arrays of multi-frequency structures.¹⁹ However, a direct comparison of these technologies is challenging because IM3 is measured with different Δf and the devices have different Q s. To adjust for these variations, Δf can be divided by the full-width-at-half-maximum (FWHM) of the device response; devices with higher Q s provide greater rejection of the out-of-band tones, therefore, a competitive comparison between the G-RCT and a higher Q device requires that Δf be smaller as a multiple of FWHM.

Table II shows a comparison of the G-RCT and a contour mode Si-MEMS device, which demonstrates that the V_{IIP3} of the Si-MEMS device is slightly better, but the test on the G-RCT is roughly twice as stringent due to the

TABLE II. Device comparison.

	This work	Reference 19
Type	Clamped drum	Contour-mode disk
Dimensions (μm)	4×6	34 (diameter)
Gate voltage (V)	4.5	7
V_{IIP3} (dBm V)	52.1	65.0
Q	120	20 500
f_0	40 MHz	157 MHz
S_{21}	-55 dB	-50 dB
Δf (FWHM)	5 MHz = $14 \times$	200 kHz = $26 \times$

smaller Δf . S_{21} for both devices is also very similar, but the G-RCT has an advantage in that it attains this value with a lower V_{gs} . In addition, the G-RCT consumes an order of magnitude less die area even though its f_0 is lower than the Si-MEMS device, primarily due to the effect of strain engineering.

In conclusion, G-RCTs offer nearly equivalent performance to Si-MEMS in terms of their linearity and transduction strength. However, the active sensing of G-RCTs allows them to scale to higher frequencies without the increased parasitics and decreased rejection observed in Si-MEMS. Although G-RCTs are not competitive with FBARs for applications in RF front-end filters, they may find use in intermediate-frequency stages in radios where the linearity and loss requirements are less stringent, but the G-RCT's tunability and ease of integration are still of great value.

The authors like to thank Arend M. van der Zande, Frank Lane, and Victor Abramsky for critical discussions. This work was supported by the Air Force Office of Scientific Research (AFOSR) under Grant No. FA9550-09-1-0705, by the Defense Advanced Research Projects Agency (DARPA) under U.S. Office of Naval Research Contract No. N00014-1210814, by the Qualcomm Innovation Fellowship, and by the Semiconductor Research Corporation (SRC) Nanoelectronics Research Initiative (NRI) through the INDEX Center.

¹G.-H. Lee, R. C. Cooper, S. J. An, S. Lee, A. van der Zande, N. Petrone, A. G. Hammerberg, C. Lee, B. Crawford, W. Oliver *et al.*, *Science* **340**, 1073 (2013).

²S. Lee, C. Chen, V. V. Deshpande, G.-H. Lee, I. Lee, M. Lekas, A. Gondarenko, Y.-J. Yu, K. Shepard, P. Kim *et al.*, *Appl. Phys. Lett.* **102**, 153101 (2013).

³Y. Oshidari, T. Hatakeyama, R. Kometani, S. Warisawa, and S. Ishihara, *Appl. Phys. Express* **5**, 117201 (2012).

⁴M. Lekas, S. Lee, C. Chen, W.-J. Cha, K. Ayyagari, J. Hone, and K. Shepard, in *European Frequency and Time Forum International Frequency Control Symposium (EFTF/IFC), 2013 Joint* (2013), p. 543.

⁵A. Newaz, Y. S. Puzyrev, B. Wang, S. T. Pantelides, and K. I. Bolotin, *Nat. Commun.* **3**, 734 (2012).

⁶Y. Xu, O. Li, and R. Xu, in *2013 IEEE International Wireless Symposium (IWS)* (2013), pp. 1–6.

⁷R. Marathe, B. Bahr, W. Wang, Z. Mahmood, L. Daniel, and D. Weinstein, *J. Microelectromech. Syst.* **23**, 636 (2014).

⁸A. M. van der Zande, R. A. Barton, J. S. Alden, C. S. Ruiz-Vargas, W. S. Whitney, P. H. Q. Pham, J. Park, J. M. Parpia, H. G. Craighead, and P. L. McEuen, *Nano Lett.* **10**, 4869 (2010).

⁹R. A. Barton, B. Ilic, A. M. van der Zande, W. S. Whitney, P. L. McEuen, J. M. Parpia, and H. G. Craighead, *Nano Lett.* **11**, 1232 (2011).

¹⁰C. Chen, S. Rosenblatt, K. I. Bolotin, W. Kalb, P. Kim, I. Kymissis, H. L. Stormer, T. F. Heinz, and J. Hone, *Nat. Nanotechnol.* **4**, 861 (2009).

- ¹¹P. Weber, J. Guttinger, I. Tsioutsios, D. E. Chang, and A. Bachtold, *Nano Lett.* **14**, 2854 (2014).
- ¹²A. Eichler, J. Moser, J. Chaste, M. Zdrojek, I. Wilson-Rae, and A. Bachtold, *Nat. Nanotechnol.* **6**, 339 (2011).
- ¹³Z. Wang and P. X.-L. Feng, *Appl. Phys. Lett.* **104**, 103109 (2014).
- ¹⁴C. Chen, S. Lee, V. V. Deshpande, G.-H. Lee, M. Lekas, K. Shepard, and J. Hone, *Nat. Nanotechnol.* **8**, 923 (2013).
- ¹⁵F. Bi and B. Barber, *IEEE Microwave Mag.* **9**, 65 (2008).
- ¹⁶L. D. Landau and E. M. Lifshitz, *Theory of Elasticity*, A Course of Theoretical Physics Vol. 7 (Pergamon Press, 1970), p. 46.
- ¹⁷S. Timoshenko and S. Woinowsky-Krieger, *Theory of Plates and Shells* (McGraw-Hill, New York, 1959), Vol. 2.
- ¹⁸C. Chen, Ph.D. dissertation, Columbia University, 2013.
- ¹⁹Y.-W. Lin, S.-S. Li, Z. Ren, and C. T.-C. Nguyen, in *Proceedings of IEEE International Ultrasonics Symposium, Rotterdam, Netherlands* (2005), p. 1592.
- ²⁰R. Navid, J. R. Clark, M. Demirci, and C.-C. Nguyen, in *14th IEEE International Conference on Micro Electro Mechanical Systems, 2001 (MEMS 2001)* (IEEE, 2001), p. 228.
- ²¹Y. Xu, C. Chen, V. V. Deshpande, F. A. DiRenno, A. Gondarenko, D. B. Heinz, S. Liu, P. Kim, and J. Hone, *Appl. Phys. Lett.* **97**, 243111 (2010).
- ²²R. Lifshitz and M. Cross, in *Reviews of Nonlinear Dynamics and Complexity, Vol. 1*, edited by H. G. Schuster (Wiley, 2008), p. 10.
- ²³E. Tholén, Ph.D. dissertation, KTH School of Engineering Sciences, Stockholm, 2009.